Bulletin of the Seismological Society of America, Vol. XX, No. XX, pp. –, – 2018, doi: 10.1785/0120170305

Landslides Triggered by the 14 November 2016 M_w 7.8 Kaikoura Earthquake, New Zealand

by C. Massey, D. Townsend, E. Rathje, K. E. Allstadt, B. Lukovic, Y. Kaneko, B. Bradley, J. Wartman, R. W. Jibson, D. N. Petley, N. Horspool, I. Hamling, J. Carey, S. Cox, J. Davidson, S. Dellow, J. W. Godt, C. Holden, K. Jones, A. Kaiser, M. Little, B. Lyndsell, S. McColl, R. Morgenstern, F. K. Rengers, D. Rhoades, B. Rosser, D. Strong, C. Singeisen, and M. Villeneuve

Abstract The 14 November 2016 M_w 7.8 Kaikoura earthquake generated more than 10,000 landslides over a total area of about 10,000 km^2, with the majority concentrated in a smaller area of about 3600 km^2. The largest landslide triggered by the earthquake had an approximate volume of 20($\pm$2) M m^3, with a runout distance of about 2.7 km, forming a dam on the Hapuku River. In this article, we present version 1.0 of the landslide inventory we have created for this event. We use the inventory presented in this article to identify and discuss some of the controls on the spatial distribution of landslides triggered by the Kaikoura earthquake. Our main findings are (1) the number of medium to large landslides (source area $\geq$ 10,000 m^2) triggered by the Kaikoura earthquake is smaller than for similar-sized landslides triggered by similar magnitude earthquakes in New Zealand; (2) seven of the largest eight landslides (from 5 to 20 M m^3) occurred on faults that ruptured to the surface during the earthquake; (3) the average landslide density within 200 m of a mapped surface fault rupture is three times that at a distance of 2500 m or more from a mapped surface fault rupture; (4) the "distance to fault" predictor variable, when used as a proxy for ground-motion intensity, and when combined with slope angle, geology, and elevation variables, has more power in predicting landslide probability than the modeled peak ground acceleration or peak ground velocity; and (5) for the same slope angles, the coastal slopes have landslide point densities that are an order of magnitude greater than those in similar materials on the inland slopes, but their source areas are significantly smaller.

Introduction

The 14 November 2016 M_w 7.8 Kaikoura earthquake in New Zealand occurred at 12:03 a.m. local time (Kaiser *et al.*, 2017). The epicenter was located about 4 km from the rural town of Waiau (population 250) in north Canterbury (Fig. 1), with rupture initiation at a shallow depth of 14.1 km (Nicol *et al.*, 2018). Large shallow earthquakes in mountain chains typically trigger substantial numbers of landslides (Hovius *et al.*, 1997; Parker *et al.*, 2011; Hancox *et al.*, 2014, 2016; Xu *et al.*, 2016). The Kaikoura earthquake (Dellow *et al.*, 2017) triggered more than 10,000 landslides over an area of about 10,000 km^2, with the majority being focused in an area of about 3600 km^2 (Fig. 1). Fortunately, the area affected by landslides is comparatively remote and sparsely populated such that only a few dwellings were impacted by landslides, and there were no recorded landslide-related fatalities (Stevenson, 2017). However, the landslides dammed rivers, blocked roads and railways, and disrupted agricultural land throughout this region. Landslides along the coast caused substantial damage to both State Highway (SH) 1 and the northern section of the South Island Main Trunk Railway, blocking both in multiple locations (Davies, 2017). At the time of writing, the section of SH1 north of Kaikoura is due to reopen on 15 December 2017, over a year after the earthquake.

The long-term stability of damaged but as yet unfailed slopes is a cause for concern in light of the risk of future strong earthquakes and significant precipitation events. This has been exemplified by debris flows and floods that occurred during rain associated with cyclones Debbie (23 March to 7 April 2017) and Cook (14 April 2017), which caused several of the dams to breach, releasing debris flows and floods that traveled several kilometers downstream. Debris flows were also triggered on the steep coastal cliffs north and south of Kaikoura, leading to the intermittent closures of the reopened portion of SH1 south of Kaikoura.

Both the number of landslides and the area affected are much less than expected, based on worldwide observations, for an earthquake of this magnitude (Keefer, 2002; Malamud

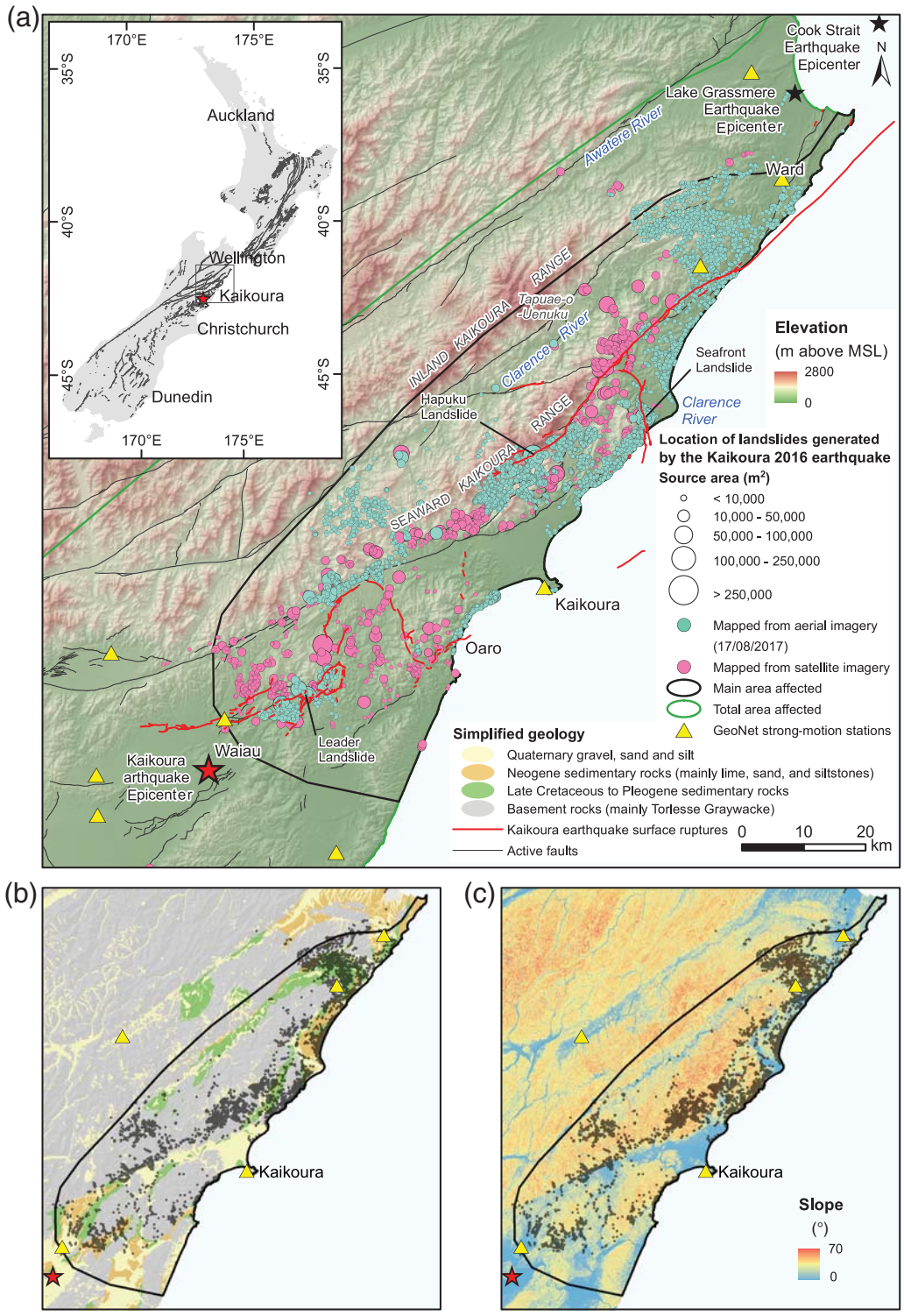

Figure 1. (Inset) The area of New Zealand affected by coseismic landslides triggered by the 2016 M_w 7.8 Kaikoura earthquake. (a) The mapped 10,195 coseismic landslide source areas and their size (area) triggered by the earthquake, superimposed on the 8 by 8 m digital elevation model (DEM) for New Zealand, classified by elevation in meters above sea level. (b) The landslide source area distribution overlain on the main geological units. (c) Landslide source area distribution shown on the 8 m ground resolution DEM for New Zealand.

et al., 2004). To investigate the reason for this, we analyze an inventory we are creating for landslides triggered by this earthquake; our analysis relates the spatial distribution and size characteristics of the triggered landslides to geology, topography, strong shaking, and other geologic factors. The objective of this article is to describe these characteristics of the triggered landslides and quantify their relationship to the various causative factors.

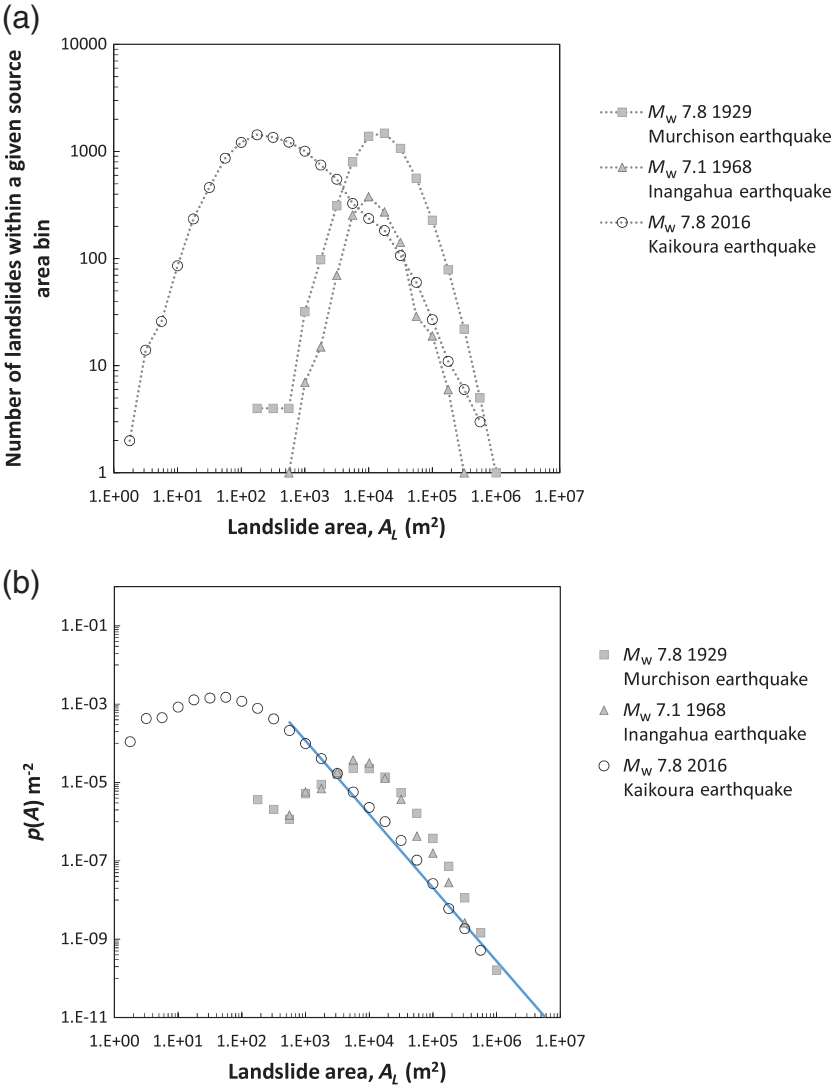

Figure 2. (a) The number of landslides (frequency) with source areas within each source-area bin. Landslide source-area bin widths are equal in logarithmic space for all data sets. (b) Landslide probability density plotted against landslide area (for the landslide source areas only), for landslides generated by the Kaikoura earthquake, the 1968 M_w 7.1 Inangahua, New Zealand, earthquake (Hancox *et al.*, 2014) and the 1929 M_w 7.8 Murchison, New Zealand, earthquake (Hancox *et al.*, 2016). For (b), the power-law fitting statistics are (1) the 2016 M_w 7.8 Kaikoura earthquake, in which $N_{LT} = 10{,}195$, $x_{min} = 500$ m^2, and $\alpha = 1.88$; (2) the 1929 M_w 7.8 Murchison earthquake (Hancox *et al.*, 2016), in which $N_{LT} = 6104$, $x_{min} = 10{,}000$ m^2, and $\alpha = 2.62$; and (3) the 1968 M_w 7.1 Inangahua earthquake (Hancox *et al.*, 2014), in which $N_{LT} = 1199$, $x_{min} = 10{,}000$ m^2, and $\alpha = 2.71$.

A broad-based investigation of the triggered landslides began immediately following the earthquake. Dellow *et al.* (2017) provide a preliminary description of the landslides triggered by this earthquake and the immediate response to document them and evaluate related hazards. Jibson *et al.* (2017) give an overview of landslide types and distribution accompanied by illustrations of the triggered landslides. In this article, we present version 1.0 of the landslide inventory we created for this event, which builds on the earlier preliminary inventories presented by Rathje *et al.* (2017) and Dellow *et al.* (2017). Refer to Data and Resources for instructions about how to access this data set. We present these findings as a preliminary account of the potential controls we have observed on the landslide distribution triggered by this event. It is version 1.0, because mapping is ongoing in those areas where the landslide distribution was initially mapped from satellite images. The high-resolution orthorectified aerial photographs that have been used to map much of the distribution were not available in these areas at the time of publication.

Detailed Landslide Inventory from Mapping

Previous studies of worldwide earthquakes have related earthquake magnitude to the number of landslides. For an M_w 7.8 earthquake, the relationship of Malamud *et al.* (2004) predicts about 25,000 landslides and the relation of Keefer (2002) predicts about 60,000 landslides. Both relations are based solely on magnitude and do not consider other factors such as earthquake depth, distance to fault, topography, rock type, climate, and vegetation that contribute to landslide occurrence. These estimates based on worldwide earthquakes are two to six times higher than the approximate 10,000 landslides mapped thus far from the Kaikoura earthquake.

The version 1.0 landslide inventory contains 10,195 coseismic landslides (Figs. 1 and 2). These landslides are inferred to have been triggered by the Kaikoura earthquake and associated aftershocks because no major rain events occurred in the period between the earthquake and the first low-level aerial photograph survey after the earthquake, dated December 2016, used to map the distribution.

To map the distribution, we primarily used postearthquake 0.3 m ground resolution orthorectified air photographs, and digital surface models derived from them, alongside digital elevation models (DEMs) from postearthquake airborne light detection and ranging (lidar) surveys, and other pre- and post-Kaikoura earthquake imagery and lidar data (these data sets are described in Table A1). Landslides were manually digitized directly into a Geographic Information Systems. This was done because the outputs from the automated landslide detection tools we

ran generally performed poorly. They (1) wrongly identified areas of high albedo (in the images) as landslide sources, for example, identified bare farmland; (2) created multiple landslide source regions for individual landslide sources and vice versa where large sources were in fact multiple individual landslides; and (3) required significant time to manually edit. Several authors have shown how landslide mapping can influence an inventory and therefore the results of any analyses of it. For example, Parker *et al.* (2011) report more than 56,000 landslides for the 2008 M_w 7.9 Wenchuan, China, earthquake, but Xu *et al.* (2014, 2016) report 196,007 mapped landslides and Li *et al.* (2014) report 57,150 landslides. Li *et al.* (2014) attribute their increase in numbers over Parker *et al.* (2011) to their separating individual landslides from amalgamated clusters. This change increased the number of mapped landslides but decreased the total volume reported; for example, see Li *et al.* (2014). Because of such issues, we did not use the results of any of the automated landslide-detection algorithms. Low-level orthorectified aerial photographs taken in 2015, before the earthquake, were used to identify the many pre-earthquake landslides in the region, to ensure that such landslides were not attributed to the earthquake. We also relied on the geotagged oblique air photos taken from multiple postearthquake helicopter reconnaissance missions to support and verify mapping in areas of complex terrain. The landslide mapping was carried out by experienced landslide researchers using the scheme outlined by Dellow *et al.* (2017). Where possible, we separated the landslide source area from the debris trail to allow more accurate estimates of landslide size. This was done using a combination of aerial images, pre- and postearthquake ground surface difference models derived from lidar and photogrammetry, and shade models generated from them, which helped define landslide morphology. We used the scheme of Hungr *et al.* (2014) to classify the landslides by their mechanism and dominant material type. To date, the smallest mapped landslide source area is about 5 m^2 and the largest is about 550,000 m^2. Refinement of the inventory, in particular at the lower end of the size range, is ongoing. The number of mapped landslides (frequency) with source areas of a given size has been binned using source area bin widths that are equal in logarithmic space (Fig. 2a). As expected, the areas of the landslide sources generated by this event exhibit characteristic power-law scaling (Fig. 2b; e.g., Hovius *et al.*, 1997; Guzzetti *et al.*, 2002; Malamud *et al.*, 2004; Parker *et al.*, 2015), defined by

$$p(A_L) = \frac{1}{N_{LT}} \times \frac{\delta N_L}{\delta A_L}, \quad (1)$$

in which $p(A_L)$ is the probability density of a given area within a near-complete inventory—defined as the frequency density of landslides of a given source area bin (A_L), divided by the total number of landslides in the inventory—N_{LT} is the total number of landslides in the inventory, and δN_L is the number of landslides with areas between A_L and $A_L + \delta A_L$. For the landslide area bins, we adopted bin widths (δA_L) that increased with increasing landslide source area (A_L), so that bin widths were equal in logarithmic space. The position of the characteristic rollover (Fig. 2b) for smaller landslides occurs at a landslide source area of about 50–100 m^2. The frequency–area distributions of most landslide inventories exhibit a rollover at smaller landslide sizes for various reasons, one of which is mapping resolution (Stark and Hovius, 2001).

The power-law scaling exponent (α) of 1.88, fitted to the Kaikoura landslide distribution using the method of Clauset *et al.* (2009), with $x_{min} = 500$ m^2, falls within the range of previously observed values of landslide inventories (1.4–3.4), but it is below the central tendency of 2.3–2.5 (Van Den Eeckhaut *et al.*, 2007; Stark and Guzzetti, 2009). Figure 2 shows the landslide frequency and probability density versus area distributions for comparable inventories of landslides triggered by other notable earthquakes in New Zealand. These are (1) the 1929 M_w 7.8 Murchison earthquake (Hancox *et al.*, 2016), in which $N_{LT} = 6104$, $x_{min} = 10{,}000$ m^2, and $\alpha = 2.62$; and (2) the 1968 M_w 7.1 Inangahua earthquake (Hancox *et al.*, 2014), in which $N_{LT} = 1199$, $x_{min} = 10{,}000$ m^2, and $\alpha = 2.71$.

Our results suggest that the number of large landslides $> 10{,}000$ m^2 generated by this earthquake are less than those generated by the similar magnitude 1929 M_w 7.8 Murchison earthquake in New Zealand but are instead more comparable with those triggered by the smaller magnitude 1968 M_w 7.1 Inangahua, New Zealand, earthquake (Fig. 2a). Nevertheless, the lower α-value suggests that a higher number of larger landslides were triggered than would typically be expected given the number of smaller landslides. Such comparisons, however, do not consider differences in the physiographic setting, which could affect the numbers of landslides generated. Although a more detailed comparison of the landslides from these different earthquakes is warranted, it is currently outside the scope of this article.

The Geology and Topography of the Study Area

The region in which most of the landslides occurred can be subdivided into four main geological units (Fig. 1b and Table 1). These are described by Rattenbury *et al.* (2006), and their descriptions are summarized here in order of oldest to youngest: (1) Lower Cretaceous Torlesse (Pahau terrane) "basement" rocks formed primarily of graywacke; (2) Upper Cretaceous and Paleogene limestones, siltstones, conglomerates, and minor volcanic rocks; (3) Neogene limestones, sandstones, and siltstones; and (4) Quaternary sands, silts, and gravels. These materials and their properties tend to control the types of landslides that occurred within them. For example, the graywacke is highly jointed, and most landslides appear to be debris avalanches, controlled by multiple intersecting joint blocks, which limit the volume of such failures. Conversely, the Upper Cretaceous and Neogene

Table 1
Lithology and Landslide Types Adopted in this Article

Lithology	Proportion of Main Area Affected (%)	Landslide Point/Area Density (N/km^2)/(%)*	Dominant Landslide Types
Quaternary sands, silts, and gravels. These typically form river terrace deposits in the region	19	1.8/0.3	Debris avalanches and flows that tend to be relatively small, and their source areas are mainly located in the terrace sands and gravels on top of the steeper coastal slopes. Many other landslides occurred within the shallow regolith, which covers many slopes in the area that were affected by strong ground shaking. These include shallow translational slides in soil with displacements of a few centimeters to several meters
Neogene limestones, sandstones, and siltstones. These are typically massive, but weak rocks with unconfined compressive strengths (UCS) of typically < 2 MPa (Read and Miller, 1990)	9	5.5/0.9	Relatively shallow debris avalanches and flows that source from the more weathered rocks, or relatively deep-seated slides and slumps, where movement is thought to occur either along bedding or other persistent structural discontinuities, for example, fault planes, thin clay seams, or through the rock mass. Substantial numbers of pre-Kaikoura earthquake, large landslides were mapped in these materials of which many reactivated (a few centimeters to meters) during the earthquake, forming translational and rotational slides/slumps
Upper Cretaceous to Paleogene rocks including limestones, sandstones, siltstones, and minor volcanic rocks. These are typically massive, but weak rocks with UCS of typically < 2 MPa	12	4.6/0.5	Rockfalls and debris avalanches in areas of steeper terrain, with some slides and slumps (termed coherent after Keefer, 2013) in areas of less steep topography, and their location might be controlled by the presence of thin clay seams or small-scale changes in lithology. Several relict landslides are present in these materials, and there were numerous small rockfalls and debris avalanches from their oversteep head scarps
Lower Cretaceous Torlesse (Pahau terrane) basement rocks predominantly sandstones and argillite (graywacke). These are relatively strong rocks with UCS 10–20 MPa, but they are closely jointed	60	2.5/0.6	Rockfalls (of individual boulders) to debris and rock avalanches. Given the highly discontinuous nature of the rock mass, most landslides are controlled by multiple intersecting joint blocks, hence a potential limitation on the volume of such failures. However, the Kaikoura earthquake triggered several very large and structurally controlled rock avalanches, the Hapuku landslide being the largest mapped landslide

*Landslide point densities were calculated by dividing the number of landslide sources within a given geological unit by the area of ground within that given unit, within the main area affected by landslides (Fig. 1b). Landslide area densities were calculated by dividing the total area of all landslide sources within a given geological unit by the area of ground within that unit, within the main area affected by landslides.

sandstones and siltstone tend to be massive with highly persistent bedding planes and clay seams, which allow the development of large translational debris slides and slumps. These relationships are explained further in Table 1.

The earthquake mainly affected the northeastern portion of New Zealand's South Island. This area is dominated by the Kaikoura Ranges, which rise from sea level to a maximum elevation of 2885 m above mean sea level (amsl) at Mount Tapuae-o-Uenuku. The Kaikoura Ranges are predominantly formed of graywacke and are dissected by several large rivers. The long straight Clarence River valley separates the Seaward Kaikoura Ranges from the longer and steeper Inland Kaikoura Ranges, including Mount Tapuae-o-Uenuku. Beyond the Inland Kaikoura Range is the valley of the Awatere River, which runs parallel to that of the Clarence River. As these rivers approach the coast, the slopes reduce in gradient, where they are predominantly formed of faulted slivers of Neogene rocks and Quaternary gravel, sand, and silt. The township of Kaikoura is the largest town in the area and is located on a rocky peninsula formed of Cretaceous to Neogene sedimentary rocks and Quaternary marine terraces, about 70 km northeast of the earthquake epicenter (Fig. 1). The topography south and west of Kaikoura is relatively gentle compared with the Inland and Seaward Kaikoura Ranges. The slopes have mainly been formed by tectonically driven uplift and fluvial incision through the Neogene sandstones and siltstones, which form the main bedrock unit in the area. The climate across much of the area is temperate and it typically experiences dry cold winters.

Controls on the Spatial Distribution of Landslides

The landslide distribution does not represent a homogenous mass of landslides clustered around the earthquake epicenter. Instead, the mapped distribution shows a long generally linear pattern, with many landslides occurring on either side of the faults that ruptured to the ground surface (Fig. 1), northeast of the earthquake epicenter. Many smaller landslides concentrate along the coast and in discrete clusters on either side of the faults that ruptured. Many of the larger landslides occurred on faults with surface ruptures that passed through their source areas (Fig. 3). Interestingly, the larger landslides, while also occurring in clusters along

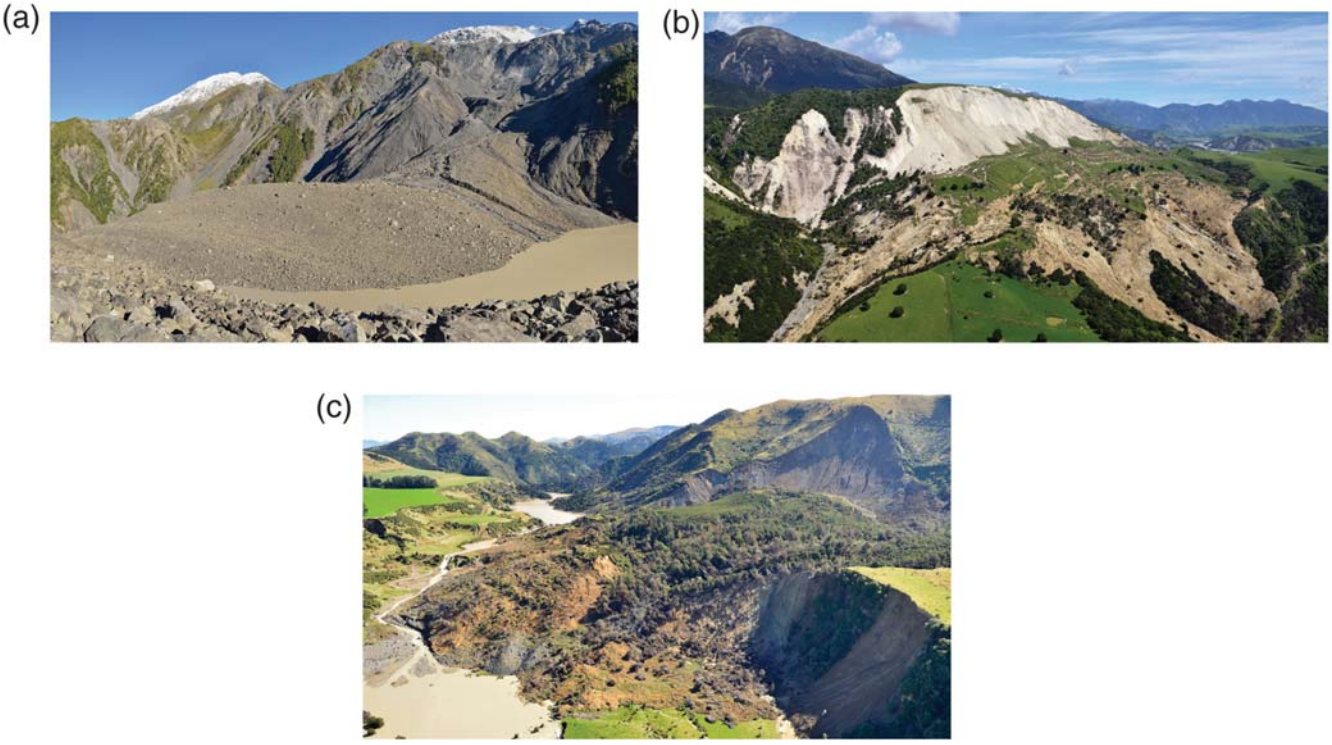

Figure 3. (a) Hapuku rock avalanche in Lower Cretaceous basement rocks—this is the largest of the mapped landslides with an estimated volume of about 20(±2) M m^3. In this case, the slide surface appears to correspond to multiple persistent discontinuities such as old and recent fault planes. Several faults that ruptured to the surface pass through the source area of the landslide. The debris left the source and blocked the Hapuku River creating a dam about 100 m high. Multiple lobes of debris of different clast size can be mapped in the deposit, indicating multiple pulses of debris deposition. The dam subsequently overtopped and the downstream face was partially eroded (due to headward erosion initiated by seepage through the dam) following Cyclone Cook in April 2017. The debris left in the source is still unstable and several debris flows have occurred, which have eroded the debris down to bedrock in places. The debris forming the dam continues to erode as water from the impounded lake flows over the crest and down the outflow channel. (b) Seafront rock slide/slump in Paleogene limestone—this is the largest mapped landslide in these materials with an approximate volume of 10(±2) M m^3. This slide surface is assumed to be deep seated (> 100 m below the surface), with the field observations and cross sections suggesting a semirotational failure through the rock mass. Much of the debris has remained intact, and so the slide/slump would be classified as coherent (Keefer, 2013). The displaced mass is still creeping and several debris flows have occurred off the toe of the intact displaced debris and also the head scarp. The Papatea fault (Hamling *et al.*, 2017) ruptured through the source area, suggesting that surface rupture of this fault caused the landslide to initiate. The vertical displacement of this fault measured ~0.5 km away from the landslide is about 6 m. We are not sure whether the landslide initiated either from permanent coseismic displacement of the ground or dynamic displacement caused by shaking, or some combination of both. (c) Leader River rock slide/slump in Neogene mudstone—the largest mapped landslide in these materials is the Leader River landslide with an approximate volume of 6(±1) M m^3. This rock slide/slump is predominantly within Neogene mudstone (including sandstone and siltstone), and the slide surface is assumed to be deep seated (about 80 m below the surface) with the displacement vectors suggesting a translational failure (with some rotation at the head scarp), possibly along bedding, which is inclined at about 20°–25° out of the slope (measured near the toe of the debris) and has the same dip direction as the vectors of landslide displacement. A faulted contact between the Lower Cretaceous graywacke and Neogene mudstone is also present in the landslide head scarp. Although there is no field evidence to suggest this contact ruptured, it is possible that a fault also ruptured through the source area of this landslide (Nicol *et al.*, 2018), but more investigation is needed to determine whether this is the case or not. (All photos by D. Townsend.)

the faults, do not appear to occur at the same locations as the clusters of smaller landslides. A comparison of the mapped distribution with the bedrock geology shows that landslide occurrence is a function of lithological variations across the area, and field observations suggest that such variations control the nature and type of landslides triggered by the earthquake (Fig. 1b and Table 1). For example, the landslide point density in the massive but weaker Neogene sandstones and siltstones is 5.5 landslides km^{-2}, compared with 2.5 landslides km^{-2} in the stronger but closely jointed graywacke (Table 1).

The dynamic response of a slope during an earthquake is not controlled solely by lithology but comprises a complex interaction between seismic waves and the hillslope (e.g., Ashford *et al.*, 1997; Sepúlveda *et al.*, 2005; Massey *et al.*, 2016; Rai *et al.*, 2016). We used our mapped landslide distribution to explore the relationships between the occurrence of a landslide and the variables that may control its occurrence (Table 2), which we have broadly grouped into: (1) predominantly landslide forcing variables representing the intensity of the event-specific seismic ground motions and their proxies, for the Kaikoura earth-

Table 2
Predictor Variables Evaluated in the Logistic Regression Model, Their ID Codes, Descriptions, and Units

Variable Type	Variable ID	Description	Units
Susceptibility	Geology 1	Quaternary sands, silts, and gravels. These materials typically form terrace deposits on the top of the steep coastal cliffs as well as inland slopes adjacent to the main rivers of the area. Many of these terraces have been incised by rivers	N/A
	Geology 2	Neogene limestones, sandstones, and siltstones, which are typically weak. They occur along sections of the coast north of Kaikoura	N/A
	Geology 3	Upper Cretaceous to Paleogene rocks including limestones, sandstones, siltstones, and minor volcanic rocks. These are typically weak (such as the Neogene limestones and sandstones) and easily erodible, and they can contain thin clay seams, which are volcanic in origin. They are typically exposed in narrow strips overlying the graywacke basement rocks	N/A
	Geology 4	Lower Cretaceous Torlesse (Pahau terrane) basement rocks are predominantly sandstones and argillite, also known as graywacke. The graywacke rocks are typically moderately well bedded and tend to be closely jointed. They form many of the coastal slopes as well as the steeper inland Kaikoura mountain ranges	N/A
	$Slope_{MEAN}$	Local hillslope gradient taken from the 8-m resolution digital elevation model (DEM) generated by GNS Science, adopting the mean value of all of the 8 m by 8 m cells that fall within each cell of the sample 32 m by 32 m grid. This variable is a proxy for the static shear stresses in the slope	Degree (°)
	$Elev_{MEAN}$	Local hillslope elevation taken from the 8-m resolution DEM generated by GNS Science, adopting the mean value of all of the 8 m by 8 m cells that fall within each cell of the sample 32 m by 32 m grid. This variable represents the observation that topography can limit the size of the landslides. For example, slopes that are higher in elevation tend to have larger surface areas and can therefore generate larger landslides than slopes at lower elevations, which tend to have smaller surface areas	m amsl
	$Curv_{PROFILE}$	Profile curvature generated using ArcGIS, taken from the curvature of the surface on a cell-by-cell basis, as fitted through that cell and its eight surrounding neighbors, using the 8-m resolution DEM generated by GNS Science. A negative value indicates the surface is upwardly convex at that cell. A positive profile indicates the surface is upwardly concave at that cell. A value of 0 indicates the surface is flat. This variable is a proxy for slope sharpness that represents topographic amplification effects, because amplification of shaking has been recorded at sharp breaks in slope (e.g., Massey *et al.*, 2016; Janku, 2017)	1/100 of a z unit
	Asp_{MEAN}	The aspect for each sample grid cell was calculated using ArcGIS using the 8-m resolution DEM generated by GNS Science, adopting the mean of all of the 8 m by 8 m cells that fall within each cell of the 32 m by 32 m sample grid	Degree (°)
Earthquake forcing	FaultDist	The distance from the centroid of each of the 32 m by 32 m sample grid cells to the nearest fault that ruptured using the mapped surface expression, taken from the GNS Science Active Faults database (Langridge *et al.*, 2016), which includes those faults that ruptured during the Kaikoura earthquake	Meters
	PGA_{SM}	Grid of the mean peak ground acceleration (PGA) derived from ShakeMap NZ (GeoNet 2016, see Data and Resources), developed by the U.S. Geological Survey (Wald *et al.*, 1999; Worden *et al.*, 2012), and calibrated for New Zealand by Horspool *et al.* (2015). Grid resolution is 1000 m by 1000 m. The PGA values were attributed to the sample grid cell, by taking the peak ground velocity (PGV) value at its centroid	g
	PGV_{SM}	Grid of the mean PGV derived from ShakeMap NZ. Grid resolution is 1000 m by 1000 m. The PGV values were attributed to the sample grid cell, by taking the PGV value at its centroid	m/s
	PGV_{LF}	Low-frequency (long-period) PGV calculated from waveforms up to 0.33 Hz, using the method described by Holden *et al.* (2017). Grid resolution is 500 m by 500 m. The PGV values were attributed to the sample grid cell, by taking the PGV value at its centroid	m/s
	$PGV_{BRADLEY}$	Grid of PGV derived from the modeling carried out by Bradley *et al.* (2017). Grid resolution is 990 m by 990 m. The PGV values were attributed to the sample grid cell, by taking the PGV value at its centroid	m/s
	PGV_{MEAN}	Mean PGV calculated for each of the sample grid cells by sampling the PGV value from each of the three PGV models model at the centroid of each sample grid, and taking the mean of the three values	m/s
	$Disp_V$	The vertical permanent tectonic displacement caused by the earthquake was taken from the 100 m by 100 m resolution 3D displacement field derived from satellite radar and Global Positioning System (GPS) data (Hamling *et al.*, 2017). This variable is a proxy for ground-shaking intensity because areas of increasing permanent tectonic displacement should correlate with increased dynamic ground shaking and inertial loading on the soil and rock masses forming the slopes, leading to an increase in landsliding	Meters

(*continued*)

Table 2 (*Continued*)

Variable Type	Variable ID	Description	Units
	$Disp_H$	The horizontal permanent tectonic displacement was calculated for each sample grid cell as the vector of the maximum x and y displacement fields taken from Hamling *et al.* (2017), 100 m by 100 m resolution 3D displacement field. As $Disp_V$, this variable is a proxy for ground-shaking intensity	Meters
	LSR	Local slope relief (LSR) calculated using focal statistics in ArcGIS. It represents the local height (and angle) of the sample grid cell. It is calculated as the difference in elevation between the lowest in elevation 8 m by 8 m grid cell, within an 80 m (ten (10) 8 m cells) radius from the centroid of the given sample grid cell, and the mean elevation of that grid cell ($Elev_{MEAN}$). This variable represents a proxy for slopes that could amplify ground shaking due to their "larger scale steepness" (larger than just a sample grid-cell size), in which larger values of LSR represent the steeper and higher slopes of the region, which can amplify ground shaking more than lower in height and less steep slopes (Ashford *et al.*, 1997; Massey *et al.*, 2016)	Meters (m)

quake; and (2) predominantly landslide susceptibility variables that capture the strength of the hillslope materials at a regional scale and the static shear stresses at the slope scale.

We used logistic regression (e.g., Von Ruette *et al.*, 2011; Parker *et al.*, 2015) to investigate the influence that the variables listed in Table 2 have on the spatial distribution of coseismic landslides attributed to the Kaikoura earthquake. The method models the influence of multiple predictor variables on a categorical response variable Y (with possible values 0 or 1) using

$$P_{LS}(Y=1) = \frac{1}{1+\exp(-(b_0+b_1x_1+b_2x_2+b_3x_3+\cdots+b_nx_n))}, \quad (2)$$

in which logistic regression is used to estimate the coefficients $(b, b_n, \ldots)$ for predicting the probability (P_{LS}) that $Y = 1$, given the values of one or more predictor variables $(x, x_n, \ldots)$. The condition $Y = 1$ corresponds to the occurrence of a landslide within a sample grid cell. The regression coefficients are estimated using a maximum-likelihood criterion.

To undertake logistic regression, we defined a sample grid at 32 m resolution, based on an 8-m ground resolution DEM, resampled from the 2012 version of the Land Information New Zealand digital elevation model for New Zealand. The 32 m grid mesh is much less than the typical hillslope lengths in the region, which can vary from 100 to $\gg$ 1000 m. For this assessment, we used only landslide source areas and not the debris trails. Landslides with areas less than 50 m^2 were removed from our data set to eliminate sample bias, because landslides smaller than this have not been systematically mapped and may be underrepresented in the inventory. Thus, we assumed that $Y = 1$ for any given sample grid cell in which its centroid falls within a landslide source area, even if the grid cell is not fully occupied by a landslide source.

The predictor variables used in this assessment were chosen based on variables previously found to influence landslide occurrence (listed in Table 2 and shown in

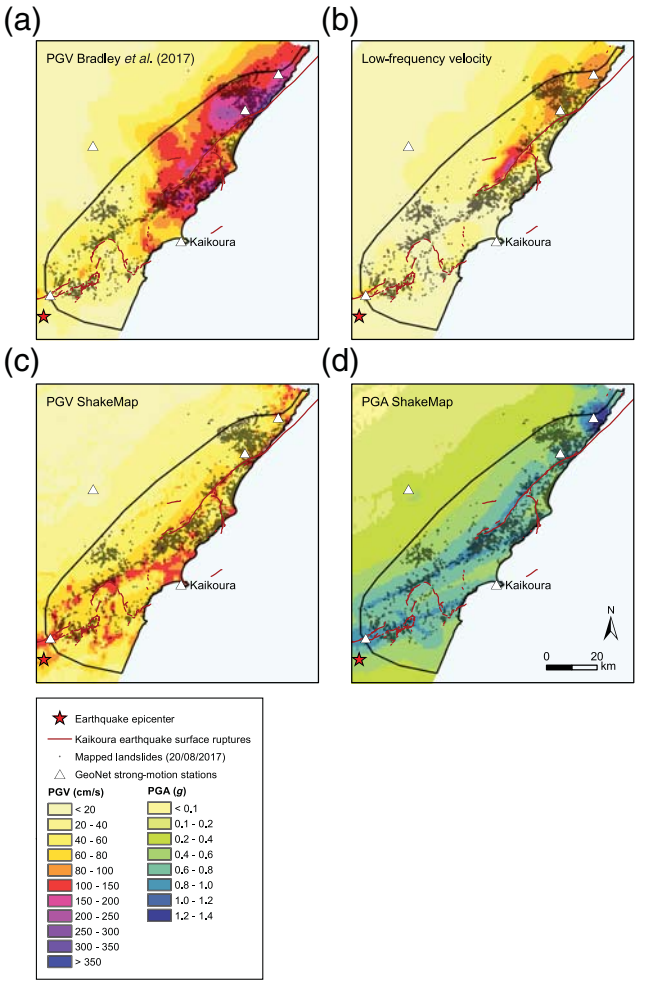

Figure 4. Peak ground velocities (PGVs) and peak ground accelerations (PGAs) from (a) Bradley *et al.* (2017) ($PGV_{BRADLEY}$), calculated up to frequencies of > 10 Hz, grid resolution 1000 m; (b) PGV_{LF}, calculated using the method by Holden *et al.* (2017) up to a frequency of 0.33 Hz, grid resolution 500 m; (c) PGV_{SM} from ShakeMap NZ (median estimates), calculated up to frequencies of 50 Hz, grid resolution 1000 m; and (d) PGA_{SM} from ShakeMap NZ (median estimates), calculated up to frequencies of 50 Hz, grid resolution 1000 m. The Kaikoura earthquake landslide distribution (shown as gray polygons, $N = 10,195$ landslides) are overlain on all the maps.

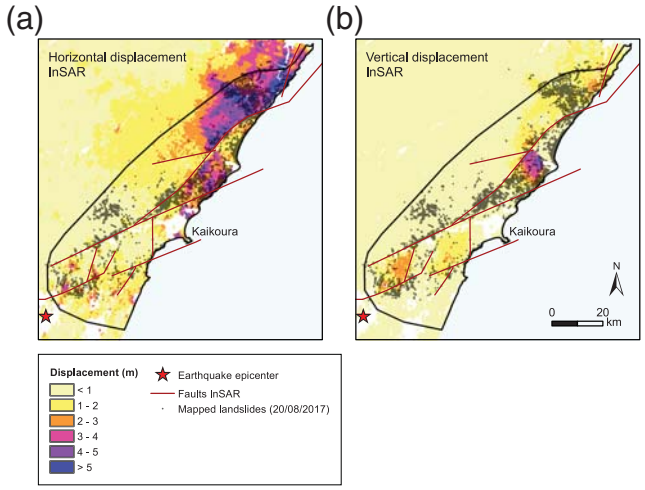

Figure 5. Permanent ground displacement: (a) horizontal and (b) vertical, and the inferred fault model taken from Interferometric Synthetic Aperture Radar (InSAR) and Global Positioning System (GPS) measurements relating to the Kaikoura earthquake presented by Hamling *et al.* (2017), grid resolution of 100 by 100 m, overlain by the Kaikoura earthquake landslide distribution (shown as gray polygons, $N = 10{,}195$ landslides).

Figs. 1b, 4, 5, and 6a–d). To represent the landslide forcing variables, we adopted (1) peak ground velocity (PGV) models, (2) peak ground acceleration (PGA) models, (3) the proximity of a landslide to a coseismic fault rupture, (4) permanent coseismic fault displacement derived from Interferometric Synthetic Aperture Radar and Global Positioning System measurements (Hamling *et al.*, 2017; Fig. 5), and (5) local slope relief (LSR). We adopted variables (1) and (2) as proxies for ground shaking, and variables (3) and (4) as less direct proxies for ground shaking. The permanent coseismic displacement variable also serves as a proxy for other susceptibility factors such as rock mass damage and steeper and higher relief. This is because displacement can lead to rock mass deformation, and displacement in a vertical sense (uplift) is usually associated with reverse-fault hanging walls, which in the Kaikoura region is where the steeper slopes are located. The proximity to a fault is inherently included in the estimation of PGV and PGA; however, we included it separately to examine the influence of local ground deformation and other near-field effects that might not be fully taken into account in the ground-motion models. To include this in the model, we determined the horizontal distance of each sample grid cell to the surface projection of the nearest fault that ruptured to the surface. These faults are different than the locations of the simplified faults used in the Hamling *et al.* (2017) fault model, and its variations, which was used in the ground-motion modeling of PGA and PGV. It should also be noted that the proximity to fault variable does not account for faults that did not rupture to the surface, but which also contribute to the shaking intensity. The location of those faults that ruptured to the surface during the earthquake was taken

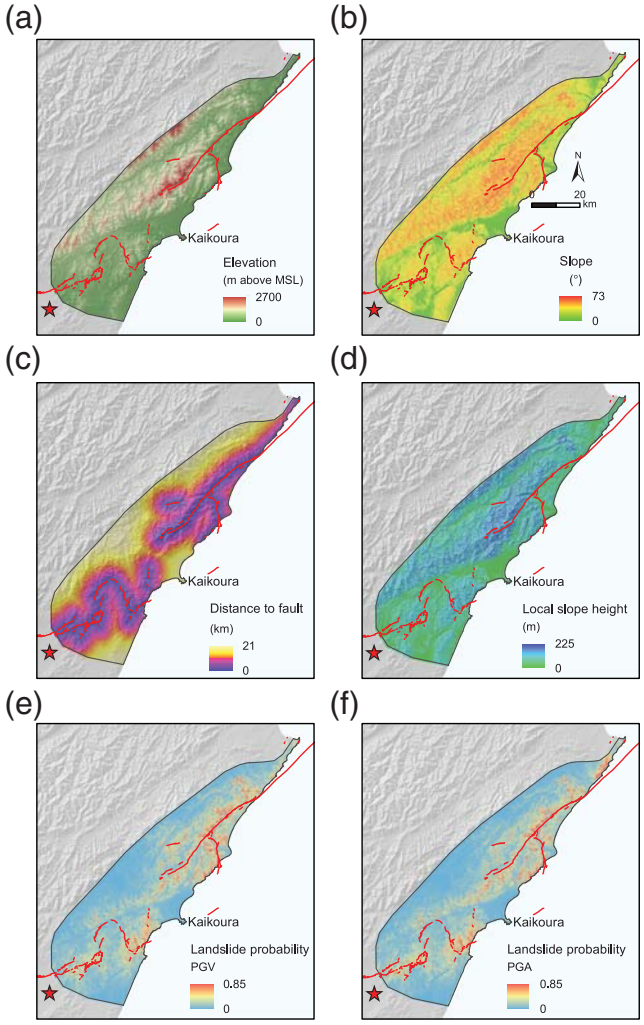

Figure 6. Maps (a–d) show the distributions of the main susceptibility predictor variables used in the logistic regression model: (a) elevation ($Elev_{MEAN}$), (b) slope ($Slope_{MEAN}$), (c) distance to fault (FaultDist), and (d) local slope relief (LSR). Maps (e,f) show the estimated landslide probabilities (P_{LS}) from the logistic regression model: (e) adopting the PGA_{SM} variable as the input ground motion and (f) adopting the PGV_{SM} variable as the input ground motion. The faults that ruptured to the surface during the earthquake are shown as red lines.

from the GNS Science Active Faults database (Langridge *et al.*, 2016; Stirling *et al.*, 2017; Litchfield *et al.*, 2018). LSR was defined as the maximum height difference within a fixed 80 m radius of the centroid of a given grid cell. It represents a proxy for slopes that could amplify ground shaking due to their "larger-scale relief" (larger than just a sample grid cell size), where larger values of LSR represent the steeper and higher slopes of the region, which can amplify ground shaking more than lower-in-height and less steep slopes (Ashford *et al.*, 1997; Massey *et al.*, 2016; Rai *et al.*, 2016; see Table 2 for details). We also used slope aspect to investigate directivity effects caused by the earthquake-rupture sequence on landslide occurrence; refer to Table 2 for details.

To estimate the PGV and PGA variables, we used three different ground-motion models, as follows: (1) $PGV_{BRADLEY}$ from Bradley *et al.* (2017); (2) PGV_{LF}, which is low-frequency (long-period) PGV calculated up to 0.33 Hz, and derived using the method described by Holden *et al.* (2017); (3) PGA_{SM} and PGV_{SM} from ShakeMap NZ (listed in Data and Resources), developed by the U.S. Geological Survey (Wald *et al.*, 1999; Worden *et al.*, 2012), and calibrated for New Zealand by Horspool *et al.* (2015) (Fig. 4c,d). The first two models incorporate directivity and basin amplification effects using 3D velocity models and account for along-strike variations in fault slip, whereas the third does not directly account for any of those effects except where they are captured by felt reports or seismic data. All three ground-motion models are based on the fault-source model of Hamling *et al.* (2017). All models use the strong-motion data for the earthquake recorded by the GeoNet strong-motion stations located within the area affected (Figs. 1 and 4). However, there were only four stations within the 3600 km^2 main area that was affected by landslides, about one station for every 900 km^2, and 13 in the wider area that was affected (10,000 km^2), about one station for every 800 km^2. The minimum, maximum, and mean distances between these stations were 6.5, 51.3, and 23.6 km, respectively, indicating a sparse coverage of stations for the main area affected by landslides.

We used landslide susceptibility variables of (1) elevation, (2) slope curvature, and (3) geology. Curvature was used as a proxy to represent potential slope-scale patterns of topographic amplification that tend to occur at breaks in slope (Ashford *et al.*, 1997; Rai *et al.*, 2016) and localized slope morphology that could represent pre-earthquake landslide scarps and therefore potentially unstable slopes, thus representing both a susceptibility and earthquake forcing variable. Curvature is scale dependent and will vary as a result of both the size of the landslide and the slope. For this article, curvature was calculated using ArcGIS and taken from the curvature of the surface on a cell-by-cell basis, as fitted through that cell and its eight surrounding neighbors. This appeared to best capture the more significant breaks in slope relative to the scale of the morphology of the slopes along the coast and inland, but not the higher peaks of the Kaikoura Ranges. Further work is needed to investigate the scale dependency of slope curvature and its effects on landslide occurrence. Slope gradient and elevation of each 32-m sample grid cell were measured by taking the mean values from the $n = 16, 8 \times 8$ m grid cells that fell within it. Table 2 details how these variables were calculated. We used a categorical variable to represent the main geological units present in the area (Table 1 and summarized in Table 2), adopting four categories.

Model fitting was done manually using the Statistica software (see Data and Resources). For a predictor variable to be included in the model, it must have a logical and statistically significant influence on P_{LS}. We used a significance level (p-value) of $p < 0.05$ (using the Wald statistic) as the threshold for inclusion in the model. During model fitting, multiple variable combinations were iteratively tested. To ensure that the predictor variables included in the model do not exhibit multicollinearity, we used a variance inflation factor (VIF) matrix, given as

$$\mathrm{VIF} = \frac{1}{1 - R^2}, \tag{3}$$

in which R^2 is the linear coefficient of determination of the relationship between any pair of predictor variables. Pairs with VIF > 10, indicating a high level of multicollinearity, are avoided in our models (Kutner *et al.*, 2004; Parker *et al.*, 2015; Table A2). The final models represent those variables that produced the best fit while meeting the significance level and multicollinearity criteria.

Results

We independently derived two models—one adopting PGA_{SM} and one adopting PGV_{SM} as the ground-motion parameter—to hindcast the probability of a landslide occurring in each grid cell. Landslide probability (P_{LS}) is given by the following equation for PGA:

$$P_{LS} = \frac{1}{1 + \exp\left(-\left(\begin{array}{c} C_{\mathrm{Intercept}} + C_{\mathrm{PGA_{SM}}} \times \mathrm{PGA_{SM}} + C_{\mathrm{FaultDist}} \times \mathrm{FaultDist} + C_{\mathrm{Elev_{MEAN}}} \times \mathrm{Elev_{MEAN}} \\ + C_{\mathrm{Slope_{MEAN}}} \times \mathrm{Slope_{MEAN}} + C_{\mathrm{LSR}} \times \mathrm{LSR} + C_{\mathrm{Geology}_X} \end{array}\right)\right)}, \tag{4}$$

in which the regression coefficients are denoted by c. The regression coefficients and goodness-of-fit statistics are shown in Tables 3 and 4 for models adopting PGA_{SM} and PGV_{SM} as the ground-motion predictor variables. We found that the best combinations of predictor variables used to estimate landslide probability were regional ground-motion models (PGA_{SM} or PGV_{SM}), distance to the surface expression of a fault that ruptured, slope gradient, elevation, LSR, and geology. All the other variables tested during model fitting were found to be less effective predictors than those included in the models, or they failed either the statistical significance test ($p < 0.05$) or the VIF test.

Figure 6e,f shows the spatial distribution of P_{LS} calculated using the two regression models (Tables 3 and 4). The only difference between the combinations of variables used

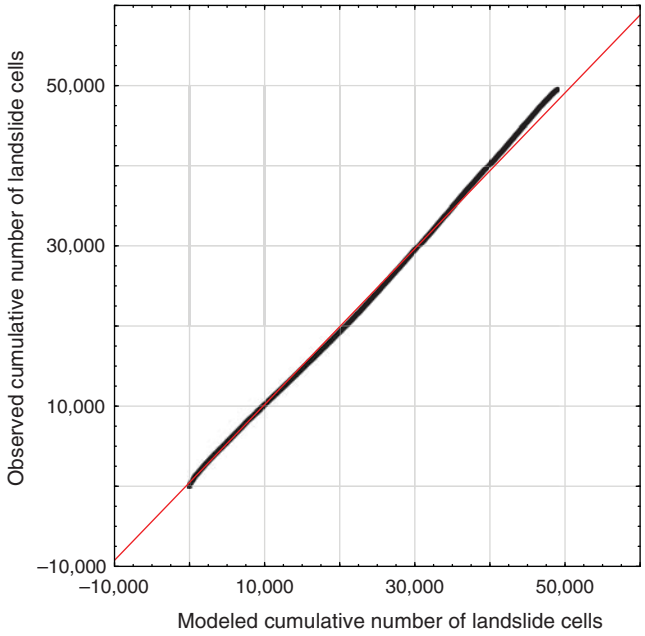

Figure 7. Consistency of the logistic regression model probabilities with the data, adopting the variables listed in Table 3 and ground-motion parameter PGV_{SM}. The graph shows a comparison of observed and predicted landslide probabilities, calculated by accumulating (adding) the predicted landslide probability (P_{LS}) values for each sample grid cell from smallest to largest, along with the corresponding observed Y-value for the same grid cell.

in each model is the ground-motion parameter (PGA_{SM} and PGV_{SM}). The results show that there is little statistical (Tables 3 and 4) or spatial (Fig. 6e,f) difference between the model outputs of P_{LS}. There was also little difference in the modeled P_{LS}, when substituting other ground-motion variables ($PGV_{BRADLEY}$, PGV_{LF}, and PGV_{MEAN}) independently in the model, while keeping the other variables fixed. To further investigate the explanatory power of the other variables on P_{LS}, we adopted a model that uses PGV_{SM} (Table 4), because the model results have a marginally higher coefficient of determination—pseudo R^2 adopting Nagelkerke's R^2 method—than those when the other PGV or PGA ground-motion variables were adopted. Although the pseudo R^2 of this model is relatively low, it is comparable with other similar studies on landslide data sets from New Zealand (Parker *et al.*, 2015).

Although the predictive power of the model on P_{LS} is low, it has no apparent biases in any part of its range. Figure 7 presents a comparison of observed versus predicted P_{LS}. This relationship was calculated by accumulating (adding) the predicted P_{LS} values for each sample grid cell from smallest to largest, along with the corresponding observed Y-value for the same grid cell. For the PGA_{SM} and PGV_{SM} models, the observed and predicted probabilities display a good fit to the line of equality. This shows that the modeled probabilities are broadly consistent with the data. The low pseudo R^2 of the model indicates that there are many landslides in cells with low values of P_{LS}. For example, the model adopting PGV_{SM} has about 43,100 cells that are classified as landslides ($Y = 1$) in which the modeled landslide probability is $\leq 10\%$. However, there are over 3.4 M cells for which the modeled probability of a landslide occurring is less than 10%, resulting in a landslide pixel density of about 0.005 landslides per cell. Conversely, there are only 228 pixels for which the modeled landslide probability is $> 50\%$, of which 26 are classified as being landslides, resulting in a landslide pixel density of 0.11.

Figure 8 shows the predictor variables in rank order of significance, which we determined by sequentially removing each of the predictor variables that contribute least to the fit of the models. In each model, and in order of importance, the slope angle, distance to fault, elevation, and geology variables contribute most to the fit of the models, followed by PGV_{SM} (or PGA_{SM} when substituted for PGV_{SM} in the model) and

Table 3
Logistic Regression Output Coefficients and Model Fit Statistics

Variable	Coefficient (c)	Standard Error	95% Confidence Interval	
			Lower Bound	Upper Bound
Intercept	−8.2531	0.0471	−8.3454	−8.1608
PGA_{SM}	0.0278	0.0005	0.0268	0.0288
FaultDist	−0.0002	0.000003	−0.0002	−0.0002
$Elev_{MEAN}$	−0.0014	0.00002	−0.0014	−0.0013
$Slope_{MEAN}$	0.0816	0.0012	0.0793	0.0840
LSR	0.0158	0.0006	0.0146	0.0169
Geology 1	0.5813	0.0196	0.5429	0.6197
Geology 2	0.1963	0.0186	0.1599	0.2327
Geology 3	−0.1466	0.0104	−0.3117	−0.2434
Geology 4	−0.6866	0.0084	−0.7031	−0.6700

Input ground-motion variable PGA_{SM}. Binomial logistic regression—modeled probability that landslide = 1. Number of observations: 3,481,858. Likelihood ratio X^2:3.41×10^4. All variables have p-values of less than 1×10^{-8}. Pseudo R^2:0.141.

Table 4
Logistic Regression Output Coefficients and Model Fit Statistics

Variable	Coefficient (c)	Standard Error	95% Confidence Interval	
			Lower Bound	Upper Bound
Intercept	−8.5968	0.0494	−8.6937	−8.4999
PGV_{MEAN}	0.0294	0.0005	0.0284	0.0303
FaultDist	−0.0002	0.000003	−0.0002	−0.0002
$Elev_{MEAN}$	−0.0013	0.00002	−0.0013	−0.0012
$Slope_{MEAN}$	0.0835	0.0012	0.0812	0.0858
LSR	0.0158	0.0006	0.0147	0.0170
Geology 1	0.1537	0.0214	0.1117	0.1957
Geology 2	0.3005	0.0188	0.2637	0.3372
Geology 3	−0.0978	0.0174	−0.1320	−0.0636
Geology 4	−0.3563	0.0137	−0.3831	−0.3295

Input ground-motion variable PGV_{SM}. Binomial logistic regression—modeled probability that landslide = 1. Number of observations: 3,481,858. Likelihood ratio X^2:3.49×10^4. All variables have p-values of less than 1×10^{-8}. Pseudo R^2:0.144.

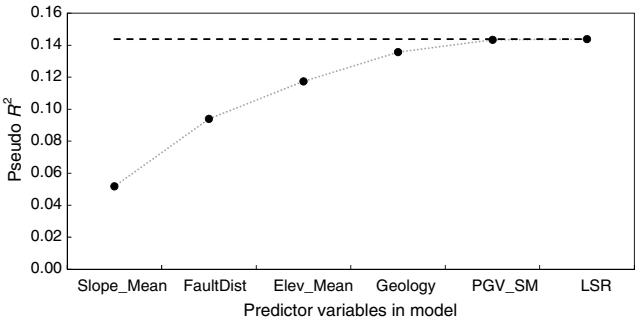

Figure 8. Logistic regression model performance adopting the variables listed in Table 4 and ground-motion parameter PGV_{SM}. The graph shows the relative contributions of predictor variable to the fit of the overall model. The sequence of model variables and the resulting pseudo R^2 values are shown in rank order of their significance, which we determined by sequentially removing each of the predictor variables contributing least to the fit of the model.

LSR. Notably, distance to the surface expression of a fault that ruptured has more explanatory power in the regression model than PGA_{SM} or PGV_{SM} ground-motion models or any of the other modeled PGV variables when tested independently within the regression model. This variable may be capturing (1) additional ground-motion parameters such as high-frequency ground motions that are not captured by the current PGA and PGV models, but which will sharply decay with distance from a fault; (2) the complex nature of the multifault rupture, and the multifrequency ground-motion intensity—and not just the higher frequency ground motions—better than the current PGA and PGV models even though it does not take into account the shaking contributed by those faults that did not rupture to the surface; and (3) the influence of rock mass damage on the rock mass strength, in which rock masses closer to faults are likely to be more jointed or damaged and have lower mass strengths than those less damaged rock masses, formed in similar materials, located farther away from faults. In addition, pre-existing persistent discontinuities such as faults and permanent tectonic surface deformation along some of them could have been important in triggering several of the large landslides located directly on or close to faults that ruptured to the surface.

The relatively low pseudo R^2 value of the model might be taken to suggest that variables not considered in the presented models might be important for predicting P_{LS}. For example, only four main geological units have been adopted even though there are significant differences in rock type and their associated physical properties within these four broad groups. Such differences in their properties have not yet been determined in sufficient detail to be included in the models. Also, the northwestern part of the main area affected by landslides contains a cluster of many small landslides (west-southwest of Ward, Fig. 1), situated in areas of Neogene mudstone. This area does not stand out in the models as having a high P_{LS}, and ground shaking (Fig. 4) was relatively low in this area during the Kaikoura earthquake with no nearby faults rupturing, which suggests that some other variable may be needed to explain this distribution. This area was affected by the 16 August 2013 M_w 6.5 Lake Grassmere earthquake and to a lesser extent by the 21 July 2013 M_w 6.6 Cook Strait earthquake (Fig. 1; Van Dissen *et al.*, 2013). The Lake Grassmere earthquake generated landslides in this area, and it induced slope cracking. Thus, the Lake Grassmere earthquake may have preconditioned the slopes in the area to fail in the subsequent Kaikoura earthquake (as described by Parker *et al.*, 2015). Alternatively, the mismatch between modeled and observed landsliding could be due to the high amplitude of the shaking in this area from the large amount of slip on the Kekerengu fault (Litchfield *et al.*, 2018), which may not be captured by the current ground-motion models.

Discussion

Kaikoura Earthquake Landslide Numbers and Their Size

Our results suggest that the number of large landslides $> 10{,}000$ m^2 generated by this earthquake is fewer than the number generated by the similar magnitude 1929 M_w 7.8 Murchison earthquake in New Zealand and similar to the number triggered by the smaller magnitude 1968 M_w 7.1 Inangahua earthquake. One reason for this might be that the area affected by strong shaking and landslides is topographically constrained. Specifically, several of the faults that ruptured to the surface extended offshore, leading to the triggering of many submarine landslides, which are not taken into account in the terrestrial landslide distribution examined in this article. Another reason for this difference may be that the Kaikoura earthquake involved the rupture of more than 20 faults that broke to the land surface over a fault-zone length of more than 100 km, suggesting that the earthquake comprised numerous subevents (Kaiser *et al.*, 2017; Stirling *et al.*, 2017) of lower magnitude (Hamling *et al.*, 2017). For each fault that ruptured, an equivalent magnitude can be calculated based on fault dimensions and estimated total slip (estimated either from geodetic and/or seismic data inversion). Hamling *et al.* (2017) estimated that the cumulative moment from the faults that ruptured south of Kaikoura equates to an M_w 7.5 earthquake. Even though the cumulative moment from the northern faults is larger than from the southern faults, the moment from some of the individual smaller faults that ruptured to the north of Kaikoura was equivalent to an M_w 7.1 earthquake (Hamling *et al.*, 2017). This would conceptually result in the shaking energy being distributed over a larger area but at a smaller amplitude and, possibly, duration. Large landslides are possibly more sensitive to shaking in the range of frequencies that often control the ground-motion PGV. If the moment release was distributed across many faults, the shaking duration and frequency content would reflect rupture from many smaller faults rather than a single large fault. Thus, the shaking would not have the same intensity as would be produced

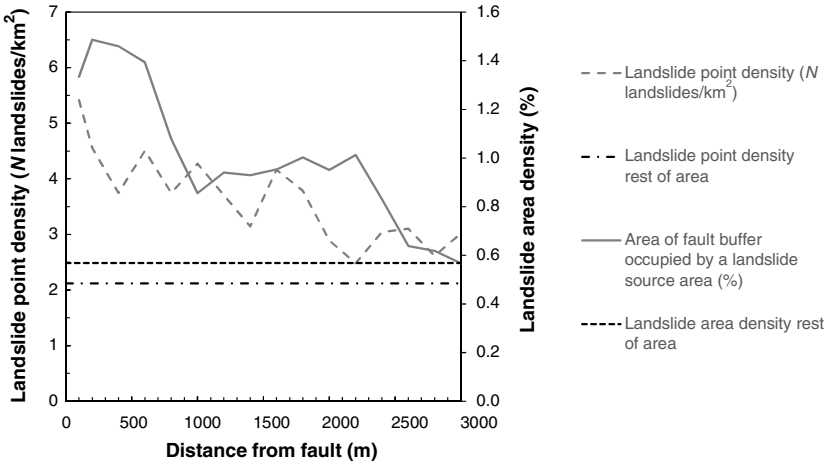

Figure 9. Landslide point and area density (N = 10,195 landslides) within each 200 m distance from fault buffer. Landslide density is calculated by taking the centroid of each landslide source area that falls within each 200 m distance buffer from the mapped surface expression of the faults that ruptured during the earthquake. The number (N) of landslide points within each distance from fault bin range is then divided by the area of slope (km^2) within each bin. The landslide area density is also shown, which is calculated in the same way as the landslide point density; however, the area of each landslide source (km^2) within each distance from fault bin is summed and divided by the total area of ground within each 200 m bin.

by a single-fault rupturing with M_w 7.8. With this in mind, it will be important to update the landslide regression models as improved ground-motion modeling data become available.

Possible Controls on the Size of the Landslides Triggered by the Earthquake

The strength of the dominant rock type in the area that was strongly shaken was mainly graywacke, and it accounts for 60% of the rocks in the main area affected by landslides. The coseismic landslide distribution in graywacke is dominated by many small landslides with few very large ones. Non-earthquake-induced landslides in such materials have in the past been limited in size as graywacke tends to be highly jointed, favoring smaller failures (Hancox *et al.*, 2015). Previous work on fracture spacing in Torlesse Schist of the Southern Alps suggests that its properties are highly influential in geomorphic response (Hales and Roering, 2009). Additional work is required to assess the landslide distribution source areas and volumes with regard to the main geological materials in which they occurred, and the role of rock mass conditioning of landslide source areas/volumes. Such an assessment is outside the scope of this current article.

Another contributing factor might be that high-frequency energy radiation during the Kaikoura earthquake is inferred by some researchers (e.g., Kaneko *et al.*, 2017) as smaller than during other landslide-triggering crustal earthquakes of a similar magnitude. Although the energy magnitude (M_e) of the Kaikoura and 2008 M_w 7.8 Wenchuan, China, earthquakes derived from low-frequency (0.5–70 s) waveforms (Incorporated Research Institutions for Seismology Data Management Center [IRIS–DMC], 2013a) are similar (M_e 7.93 and 8.06, respectively), there is a significant difference in the energy magnitudes estimated from higher frequency (0.5–2 s) waveforms (M_e 7.59 and 8.05, respectively) (IRIS-DMC, 2013b).

The Role of Distance from the Surface Fault Rupture

To explore the relationship between landslide occurrence and proximity to a surface fault rupture, we plotted the landslide point and area densities as a function of the distance from the surface expression of the nearest fault that ruptured (Fig. 9). We did this by creating successive buffer zones around the mapped fault traces that ruptured to the surface (Litchfield *et al.*, 2018; Nicol *et al.*, 2018). Then, we computed the number and total area of landslide source areas within each successive 200 m buffer to a distance of 3000 m on either side of the mapped fault trace as well as those landslide source areas through which faults pass. The density of landsliding in areas outside the fault buffers was also calculated for comparison. The results show that the landslide densities (both point and area) within 200 m of a fault are as much as three times greater than densities outside the 3000 m buffers. The results also show a general decrease in landslide density with increasing distance from a fault. At a distance of about 2500–3000 m, the background landslide density (termed "rest of area" in Fig. 9) is reached. This finding may be the result of (a) high-frequency shaking, which declines rapidly with distance from a fault, being an important control on the density of landslides triggered by the Kaikoura earthquake; (b) the rock masses close to faults being weaker because of damage from previous fault rupture events; and (c) slopes nearer faults often exhibit greater relief and are steeper than those farther away, which is the case for those slopes in the Kaikoura region. Others have reported similar findings, for example, Scheingross *et al.* (2013) hypothesized that earthflows tend to cluster near the creeping San Andreas fault because of a fault-induced zone of reduced bulk-rock strength that increases hillslope susceptibility to failure. Meunier *et al.* (2007) also suggested that near-field (near-fault) high-frequency shaking is likely to have been an important control on the density of landslides triggered by earthquakes.

Only 44 of the mapped landslide source areas are directly intersected by faults that ruptured to the surface, but this number includes seven of the eight largest landslides triggered by the Kaikoura earthquake. This would suggest that the initiation of these large landslides might have been due to a combination of pre-existing discontinuities such as

faults and rock mass damage, dynamic strong shaking, and permanent tectonic displacement of the fault as it ruptured to the surface within the source area.

Earthquake Ground-Motion Frequency, Slope Amplification, and Landsliding

As noted earlier, our logistic regression analysis indicates that PGA (or PGV when substituted for PGA in the model) from the ShakeMap NZ models performs best, but overall the PGA (or PGV) variable has low explanatory power on predicting landslide occurrence. Distance to fault, which may capture additional ground-motion parameters, has a much higher explanatory power.

Generally, the shaking nearer the source contains a lot more high-frequency energy than farther away (e.g., Davies, 2015), suggesting that ground-motion frequency may play a key role in determining slope response. Therefore, slopes that are near faults that rupture are more likely to experience such high-frequency ground motions. If the fundamental frequency of the slope is similar to the dominant frequency of the ground motion, amplification of shaking may also occur (Geli *et al.*, 1988).

Ashford *et al.* (1997) showed that the fundamental frequency (f) of a slope behind the crest can be estimated using the following equation:

$$f = \frac{4 \times H}{V_S}, \tag{5a}$$

and a slope/topographic frequency:

$$f = \frac{5 \times H}{V_S}, \tag{5b}$$

in which H is the slope height (or relief) and V_S is the shear-wave velocity of the material forming the slope. More recently, Rai *et al.* (2016) developed a model to predict the effects of topography on earthquake ground motions, adopting the relative relief of a slope (such as the LSR used in this article). For slopes in the main area affected by landslides, the mean and modal values for slope relief are 135 and 85 m for coastal slopes, and for inland slopes they are 588 and 103 m, respectively. The mean V_{S30} of the rock forming the coastal and inland slopes is estimated by Perrin *et al.* (2015) as 1000 m/s. Equation (5a) yields fundamental frequencies of the coastal slopes ranging from 1.9 to 2.9 Hz, and of the inland slopes from 0.4 to 2.4 Hz, for the mean and modal slope relief, respectively. Such fundamental frequencies are relatively high, suggesting that the combination of high-frequency shaking at close proximity to the faults, and amplification of shaking caused by the slopes responding to such high-frequency shaking, may explain why so many landslides occurred on slopes adjacent to faults. It should be noted that it is not just the fundamental frequency of the hillslope that matters, which will scale with slope morphology and relief, but also the fundamental frequency of the potential failure mass, which is likely to be shallower, and therefore have a higher fundamental frequency than the overall slope. However, such a difference may only be distinguishable from the rest of the slope if there is some pre-existing plane or damage resulting in a contrast of density/shear-wave velocity between the potential failure mass and the slope (e.g., Massey *et al.*, 2016).

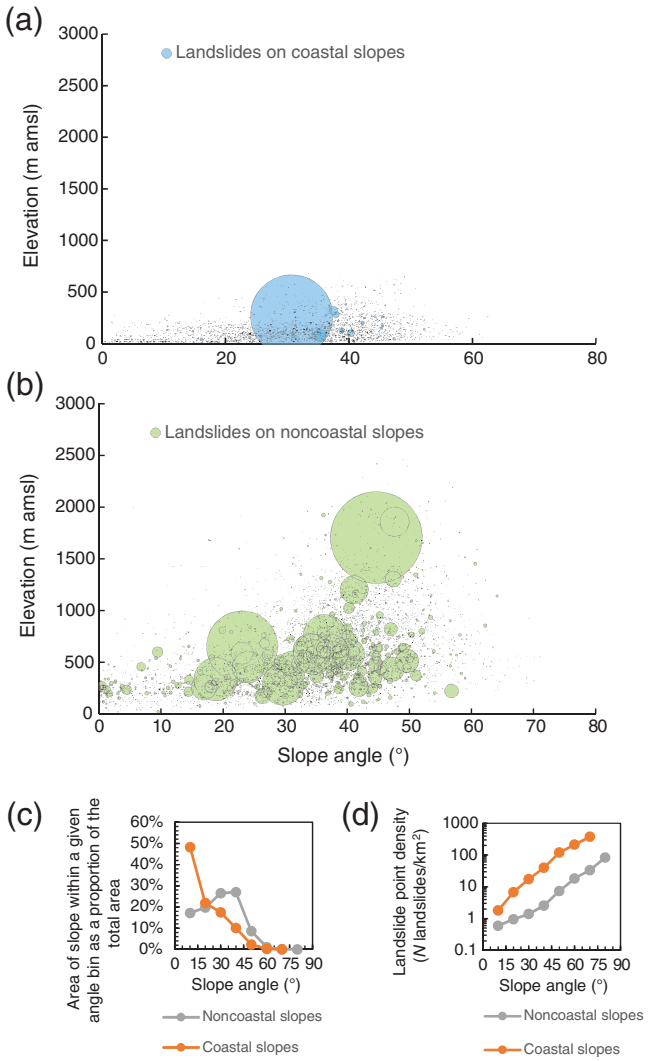

Figure 10. Landslide source areas (N = 10,195 landslides) normalized relative to the largest mapped landslide (area in km^2) and their associated elevation and slope angle taken from the 8 by 8 m New Zealand DEM. The slope angle and elevation values attributed to each landslide source area were sampled from the digital elevation grid by calculating the mean values within each source area polygon. (a) Landslides on coastal slopes only and (b) landslides on noncoastal slopes. (c) Area of slope within a given slope-angle bin as a proportion of the total area of coastal and noncoastal slopes. (d) Landslide point density for each slope-angle bin adopting 10° bins. Landslide density is calculated by taking the number of landslide sources that have mean slope angles that are within each 10° slope-angle bin range. The number (N) of landslides within each slope-angle bin range is then divided by the area of slope (km^2) within each bin. The point densities are calculated for coastal and noncoastal slopes and landslides.

Landslide Slope Angle and Elevation

We explored the higher density of landslides on the coastal slopes by attributing the centroid of each landslide source area with its mean slope angle and elevation. We split the landslide distribution into coastal and noncoastal slopes —where costal slopes are defined as those that extend from the sea to the first main inland ridge line, an approximate strip about 1 km wide—and calculated the area of coastal/noncoastal slope within each slope-angle bin (Fig. 10). The results show that coastal slopes consistently have more landslides for a given slope angle than corresponding inland slopes, but that the mean size of the landslide sources on the inland slopes is larger than those on coastal slopes. Variations in slope angle and geology cannot explain this difference because the proportion of inland slopes in the steeper slope-angle bins (Fig. 10b) is larger than the proportion of slopes on the coast within the same corresponding slope-angle bins. The coastal slopes are primarily formed from graywacke, which is also the dominant rock type forming the slopes inland. A possible explanation for these smaller landslides on the coastal slopes is that their size has been limited by the topography, as the coastal slopes have a lower relief (i.e., elevations less than 500 m amsl) compared with the higher relief slopes inland.

The results of the logistic regression model show that landslide probability increases with decreasing elevation and coastal slopes are at lower elevations. This finding could be due to the coastal-slope geometry and materials (and contrasting materials caused by coastal weathering processes and products), and their effects on amplifying the ground shaking. Studies of similar coastal slopes (Massey *et al.*, 2016), albeit in different materials, have shown that amplification—between the peak acceleration of the free-field earthquake motion and the average peak acceleration of the slope—of shaking between the base and crest of a slope could be up to 2.5 times, with a mean of 1.6 times, higher at the crest than the base of the slope. Such values are comparable with the amplification factors reported by Ashford *et al.* (1997). It is also possible that the predominantly graywacke coastal slopes are more weathered than their inland counterparts. Such hypotheses are likely to form the basis of future research on the landslides generated by the Kaikoura earthquake.

Conclusions

Our main findings are (1) the number of large landslides (with source areas $\geq$ 10,000 m^2) triggered by the Kaikoura earthquake is fewer than the number of similar sized landslides triggered by other similar magnitude earthquakes in New Zealand; (2) the largest landslides (with source volumes from 5 to 20 M m^3) occurred either on or within 2500 m of the more than 20 mapped faults that ruptured to the surface; (3) the landslide density within 200 m of a mapped surface fault rupture is as much as three times higher than those densities farther than 2500 m from a ruptured fault; (4) for the same slope angles, coastal slopes have landslide point densities that are an order of magnitude greater than those in similar materials on the inland slopes, but their source areas are significantly smaller, possibly indicating that these slopes locally amplified ground shaking, and (5) the "distance to fault" predictor variable, when used as a proxy for ground-motion intensity, has more explanatory power in predicting landslide probability than the modeled PGA or PGV variables adopted in the logistic regression modeling, even though this variable does not account for faults that did not rupture to the surface, but which also contribute to the shaking intensity. This relationship might be because the distance to fault variable captures (a) the high-frequency ground motions and their attenuation with distance from a fault better than the current PGA and PGV models; (b) the complexity of the multifault rupture, and therefore the multifrequency ground-motion intensity, better than the current PGA and PGV models; and (c) the more damaged nature of the rock masses close to the faults, where they tend to be more sheared and weakened. The strong explanatory power of the "distance to fault" predictor variable could also reflect the apparent structural control of some of the largest landslides that occur on or near faults.

Data and Resources

A recent update on information relating to submarine landslides triggered by the Kaikoura earthquake was given in the American Geophysical Union (AGU) Landslide Blog (http://blogs.agu.org/landslideblog/2017/02/27/niwa-1/, last accessed October 2017). The ShakeMap NZ map of peak ground accelerations for the Kaikoura earthquake was published online on the GeoNet website (http://www.geonet.org.nz/news/fiBIIE2uNq2qGmmiOg42m, last accessed October 2017). The software package used to carry out the logistic regression is called Statistica (http://www.statsoft.com/Products/STATISTICA-Features, last accessed October 2017). The version 1.0 landslide data set used in this article can be downloaded from the GNS Science landslide database https://data.gns.cri.nz/landslides/ (last accessed October 2017) or the https://www.designsafe-ci.org/ (last accessed October 2017) website.

Acknowledgments

The GeoNet project, the New Zealand Natural Hazards Research Platform, and GNS Science Strategic Science Investment Fund (Landslide Hazards project) funded this work. The two anonymous reviewers and Eric Thompson (U.S. Geological Survey) made some very constructive and insightful comments. Nicola Litchfield and Russ Van Dissen (GNS Science) reviewed drafts of this article. The authors would also like to thank Nicholas Sitar (University of California [UC], Berkeley, California), and Marin Clark and Dimitrios Zekkos (University of Michigan, Ann Arbor, Michigan) for the time they spent in the field with the GNS Science landslide response team. Any use of trade, firm, or product names is for descriptive purposes only and does not imply endorsement by the U.S. Government.

References

Ashford, S. A., N. Sitar, J. Lysmer, and N. Deng (1997). Topographic effects on the seismic response of steep slopes, *Bull. Seismol. Soc. Am.* **87,** 701–709.

Bradley, B. A., H. N. T. Razafindrakoto, and V. Polak (2017). Ground-motion observations from the 14 November 2016 M_w 7.8 Kaikoura, New Zealand, earthquake and insights from broadband simulations, *Seismol. Res. Lett.* **88,** 1–17.

Clauset, A., C. R. Shalizi, and M. E. J. Newman (2009). Power-law distributions in empirical data, *SIAM Rev.* **51,** 661–703, doi: 10.1137/070710111.

Davies, A. J. (2017). Transport infrastructures performance and management in the South Island of New Zealand during the first 100 days following the 2016 M_w 7.8 Kaikōura earthquake, Kaikoura earthquake special issue, *Bull. New Zeal. Soc. Earthq. Eng.* **50,** 271–298.

Davies, T. (2015). *Landslide Hazards, Risk and Disasters*, T. Davies (Volume Editor), Hazards and Disasters Series, Elsevier, Amsterdam, The Netherlands, 104 pp., ISBN: 978-0-12-396452-6.

Dellow, G. D., C. I. Massey, S. C. Cox, G. C. Archibald, J. G. Begg, Z. R. Bruce, J. M. Carey, J. Davidson, F. N. Della-Pasqua, P. Glassey, *et al.* (2017). Landslides caused by the M_w 7.8 Kaikoura earthquake and the immediate response, Kaikoura earthquake special issue, *Bull. New Zeal. Soc. Earthq. Eng.* **50,** 106–116.

Geli, L., P.-Y. Bard, and B. Jullien (1988). The effect of topography on earthquake ground motion: A review and new results, *Bull. Seismol. Soc. Am.* **78,** 42–63.

Guzzetti, F., B. D. Malamud, D. L. Turcotte, and P. Reichenbach (2002). Power-law correlations of landslide areas in central Italy, *Earth Planet. Sci. Lett.* **195,** 169–183.

Hales, T. C., and J. J. Roering (2009). A frost "buzzsaw" mechanism for erosion of the eastern Southern Alps, New Zealand, *Geomorphology* **107,** 241–253.

Hamling, I., S. Hreinsdóttir, K. Clark, J. Elliott, C. Liang, E. Fielding, N. Litchfield, P. Villamore, L. Wallace, T. J. Wright, *et al.* (2017). Complex multi-fault rupture during the 2016 M_w 7.8 Kaikoura earthquake, New Zealand, *Science* **356,** 1–16, doi: 10.1126/science.aam7194.

Hancox, G. T., N. D. Perrin, B. Lukovic, and C. I. Massey (2015). Quantifying the seismic response of slopes in Christchurch and Wellington: Wellington slope types and characterisation, *GNS Science Rept. 2013/58*.

Hancox, G. T., W. F. Ries, B. Lukovic, and R. N. Parker (2014). Landslides and ground damage caused by the M_w 7.1 Inangahua earthquake of 24 May 1968 in northwest South Island, New Zealand, *GNS Science Rept. 2014/06*.

Hancox, G. T., W. F. Ries, R. N. Parker, and B. Rosser (2016). Landslides caused by the M_w 7.8 Murchison earthquake of 17 June 1929 in northwest South Island, New Zealand, *GNS Science Rept. 2015/42*.

Holden, C., Y. Kaneko, E. D'Anastasio, R. Benites, B. Fry, and I. J. Hamling (2017). The 2016 Kaikōura earthquake revealed by kinematic source inversion and seismic wavefield simulations: Slow rupture propagation on a geometrically complex crustal fault network, *Geophys. Res. Lett.* **44,** doi: 10.1002/2017GL075301.

Horspool, N., M. Chadwick, J. Ristau, J. Salichon, and M. C. Gerstenberger (2015). ShakeMap NZ: Informing post-event decision making, *Proc. of the New Zealand Society for Earthquake Engineering Conference*, Rotorua, New Zealand, April 2015.

Hovius, N., C. P. Stark, and P. A. Allen (1997). Sediment flux from a mountain belt derived by landslide mapping, *Geology* **25,** 231–234.

Hungr, O., S. Leroueil, and L. Picarelli (2014). The Varnes classification of landslide types, an update, *Landslides* **11,** 167–194.

Incorporated Research Institutions for Seismology Data Management Center (IRIS–DMC) (2013a). *Data Services Products: Earthquake Energy & Rupture Duration*, doi: 10.17611/DP/13298836.

Incorporated Research Institutions for Seismology Data Management Center (IRIS–DMC) (2013b). *Data Services Products: Earthquake Energy & Rupture Duration*, doi: 10.17611/DP/1727715.

Janku, L. (2017). Quantification of seismic site effects on slopes in Wellington, *Ph.D. Thesis*, Department of Geological Science, University of Canterbury, New Zealand.

Jibson, R. W., K. E. Allstadt, F. K. Rengers, and J. W. Godt (2017). Overview of the geologic effects of the November 14, 2016 M_w 7.8 Kaikoura, New Zealand, earthquake, *U.S. Geol. Surv. Sci. Investig. Rept. 2017-5146*.

Kaiser, A. E., N. Balfour, B. Fry, C. Holden, N. J. Litchfield, M. C. Gerstenberger, E. D'Anastasio, N. A. Horspool, G. H. McVerry, J. Ristau, *et al.* (2017). The 2016 Kaikoura, New Zealand, earthquake: Preliminary seismological report, *Seismol. Res. Lett.* **88,** 1–13, doi: 10.1785/0220170018.

Kaneko, Y., E. Fukuyama, and I. J. Hamling (2017). Slip-weakening distance and energy budget inferred from near-fault ground deformation during the 2016 M_w 7.8 Kaikōura earthquake, *Geophys. Res. Lett.* **44,** 4765–4773, doi: 10.1002/2017GL073681.

Keefer, D. K. (2002). Investigating landslides caused by earthquakes—A historical review, *Surv. Geophys.* **23,** 473–510.

Keefer, D. K. (2013). Landslides generated by earthquakes: Immediate and long-term effects, in *Treatise on Geomorphology*, Vol. 5, Academic Press, San Diego, California, 250–266, doi: 10.1016/B978-0-12-374739-6.00091-9.

Kutner, M. H., J. Neter, and C. J. Nachtsheim (2004). *Applied Linear Regression Models*, Fourth Ed., McGraw-Hill/Irwin, New York, New York, ISBN-13: 978–0073014661.

Langridge, R. M., W. F. Ries, N. J. Litchfield, P. Villamor, R. J. Van Dissen, D. J. A. Barrell, M. S. Rattenbury, D. W. Heron, S. Haubrock, D. B. Townsend, *et al.* (2016). The New Zealand active faults database, *New Zeal. J. Geol. Geophys.* **59,** 86–96, doi: 10.1080/00288306.2015.1112818.

Li, G., J. A. West, A. L. Densmore, Z. Jin, R. N. Parker, and R. G. Hilton (2014). Seismic mountain building: Landslides associated with the 2008 Wenchuan earthquake in the context of a generalized model for earthquake volume balance, *Geochem. Geophys. Geosys.* **4,** 833–844, doi: 10.1002/2013GC005067.

Litchfield, N. J., P. Villamor, R. J. Van Dissen, A. Nicol, P. M. Barnes, D. J. A. Barrell, J. Pettinga, R. M. Langridge, T. A. Little, J. Mountjoy, *et al.* (2018). Surface fault rupture from the M_w 7.8 2016 Kaikōura earthquake, New Zealand, and insights into factors controlling multi-fault ruptures, *Bull. Seismol. Soc. Am.* doi: 10.1785/0120170300 (this issue).

Malamud, B. D., D. L. Turcotte, F. Guzzetti, and P. Reichenbach (2004). Landslide inventories and their statistical properties, *Earth Surf. Process. Landf.* **29,** 687–711.

Massey, C. I., F. N. Della-Pasqua, C. Holden, A. E. Kaiser, L. Richards, J. Wartman, M. J. McSaveney, G. C. Archibald, M. Yetton, and L. Janku (2016). Rock slope response to strong earthquake shaking, *Landslides* **14,** 249–268, doi: 10.1007/s10346-016-0684-8.

Meunier, P., N. Hovius, and J. Haines (2007). Regional patterns of earthquake-triggered landslides and their relation to ground motion, *Geophys. Res. Lett.* **34,** L20408, 1–5, doi: 10.1029/2007GL031337.

Nicol, A., N. Khajavi, J. Pettinga, C. Fenton, T. Stahl, S. Bannister, K. Pedley, N. Hyland, T. Bushell, I. Hamling, *et al.* (2018). Preliminary geometry, slip and kinematics of fault ruptures during the 2016 M_w 7.8 Kaikōura earthquake in the North Canterbury region of New Zealand, *Bull. Seismol. Soc. Am.* (this issue).

Parker, R. N., A. L. Densmore, N. J. Rosser, M. de Michele, Y. Li, R. Huang, S. Whadcoat, and D. N. Petley (2011). Mass wasting triggered by the 2008 Wenchuan earthquake is greater than orogenic growth, *Nature Geosci.* **4,** 449–452, doi: 10.1038/ngeo1154.

Parker, R. N., G. T. Hancox, D. N. Petley, C. I. Massey, A. L. Densmore, and N. J. Rosser (2015). Spatial distributions of earthquake-induced landslides and hillslope preconditioning in the northwest South Island, New Zealand, *Earth Surf. Dynam.* **3,** 501–525, doi: 10.5194/esurf-3-501-2015.

Perrin, N. D., D. Heron, A. Kaiser, and C. Van Houtte (2015). V_{S30} and NZS 1170.5 site class maps of New Zealand, *New Zealand Society for Earthquake Engineering Conference*, Rotorua, New Zealand, 10–12 April 2015, Paper Number O-07.

Rai, M., A. Rodriguez-Marek, and A. Yong (2016). An empirical model to predict topographic effects in strong ground motion using California

small- to medium-magnitude earthquake database Manisha, *Earthq. Spectra* **32,** 1033–1054.

Rathje, E., M. Little, J. Wartman, A. Athanasopoulos-Zekkos, C. Massey, and N. Sitar (2017). Preliminary landslide inventory for the 2016 Kaikoura, New Zealand earthquake derived from satellite imagery and aerial/field reconnaissance, version 1, 4 January 2017, *Quick Report 1, ver. 1 of the Forthcoming NZ–US Geotechnical Extreme Events Reconnaissance (GEER) Association Report on the Geotechnical Effects of the 2016* M_w *7.8 Kaikoura Earthquake*.

Rattenbury, M. S., D. Townsend, and M. R. Johnston (Compilers) (2006). *Geology of the Kaikoura Area: Scale 1:250,000 Geological Map*, GNS Science, Institute of Geological & Nuclear Sciences, Lower Hutt, New Zealand, scale 1:250,000 Geological Map 13, 70 pp. + 1 folded map.

Read, S. A. L., and P. J. Miller (1990). Characterisation and classification of New Zealand Tertiary age sedimentary soft rocks, in *Bridge Design and Research Seminar*, Road Engineering in Soft Rock Materials, Vol. 4, RRU Bulletin 84, 1–25.

Scheingross, J. S., B. M. Minchew, B. H. Mackey, M. Simons, M. P. Lamb, and S. Hensley (2013). Fault-zone controls on the spatial distribution of slow-moving landslides, *Geol. Soc. Am.* **125,** 473–489.

Sepúlveda, S., W. Murphy, R. W. Jibson, and D. N. Petley (2005). Seismically induced rock slope failures resulting from topographic amplification of strong ground motions: The case of Pacoima Canyon, California, *Eng. Geol.* **80,** 336–348.

Stark, C. P., and F. Guzzetti (2009). Landslide rupture and the probability distribution of mobilized debris volumes, *J. Geophys. Res.* **114,** 1–16, doi: 10.1029/2008jf001008.

Stark, C. P., and N. Hovius (2001). The characterization of landslide size distributions, *Geophys. Res. Lett.* **28,** 1091–1094, doi: 10.1029/2000GL008527.

Stevenson, J. R. (2017). Economic and social reconnaissance: Kaikōura earthquake 2016, Kaikoura earthquake special issue, *Bull. New Zeal. Soc. Earthq. Eng.* **50,** 343–351.

Stirling, M. W., N. J. Litchfield, P. Villamore, R. J. Van Dissen, A. Nicol, J. Pettinga, P. Barnes, R. M. Langridge, T. Little, D. J. A. Barrell, *et al.* (2017). The M_w 7.8 2016 Kaikoura earthquake: Surface fault rupture and seismic hazard context, *Bull. New Zeal. Soc. Earthq. Eng.* **50,** 73–84.

Van Den Eeckhaut, M., J. Poesen, G. Govers, G. Verstraeten, and A. Demoulin (2007). Characteristics of the size distribution of recent and historical landslides in a populated hilly region, *Earth Planet. Sci. Lett.* **256,** 588–603, doi: 10.1016/j.epsl.2007.01.040.

Van Dissen, R., M. McSaveney, D. Townsend, G. Hancox, T. Little, W. Ries, N. Perrin, G. Archibald, S. Dellow, C. Massey, *et al.* (2013). Landslides and liquefaction generated by the Cook Strait and Lake Grassmere earthquakes: A reconnaissance report, *Bull. New Zeal. Soc. Earthq. Eng.* **46,** 196–200.

Von Ruette, J., A. Papritz, P. Lehmann, C. Rickli, and D. Or (2011). Spatial statistical modelling of shallow landslides-validating predictions for different landslide inventories and rainfall events, *Geomorphology* **133,** 11–22.

Wald, D. J., V. Quitoriano, T. H. Heaton, H. Kanamori, C. W. Scrivner, and B. C. Worden (1999). TriNet "ShakeMaps": Rapid generation of peak ground-motion and intensity maps for earthquakes in southern California, *Earthq. Spectra* **15,** 537–556.

Worden, C. B., M. C. Gerstenberger, D. A. Rhoades, and D. J. Wald (2012). Probabilistic relationships between ground-motion parameters and modified Mercalli intensity in California, *Bull. Seismol. Soc. Am.* **102,** 204–221, doi: 10.1785/0120110156.

Xu, C., X. Xu, Y. Tian, L. Shen, Q. Yao, X. Huang, J. Ma, X. Chen, and S. Ma (2016). Two comparable earthquakes produced greatly different coseismic landslides: The 2015 Gorkha, Nepal and 2008 Wenchuan, China events, *J. Earth Sci.* **27,** 1008–1015.

Xu, C., X. Xu, X. Yao, and F. Dai (2014). Three (nearly) complete inventories of landslides triggered by the May 12, 2008 Wenchuan M_w 7.9 earthquake of China and their spatial distribution statistical analysis, *Landslides* **11,** 441–461, doi: 10.1007/s10346-013-0404-6.

Appendix

This appendix is comprised of two tables. Table A1 is a summary of the imagery and topographic data used to map version 1.0 of the landslide distribution presented in the article and Table A2 is the variance inflation factor (VIF) matrix, which was used as a method to ensure that the predictor variables included in the logistic regression model did not exhibit multicollinearity.

GNS Science
P.O. Box 30-368
Lower Hutt 5040
New Zealand
c.massey@gns.cri.nz
(C.M., D.T., B.L., Y.K., N.H., I.H., J.C., S.C., S.D., C.H., K.J., A.K., B.L., R.M., D.R., B.R., D.S., C.S.)

University of Texas
110 Inner Campus Drive
Austin, Texas 78705
(E.R., M.L.)

U.S. Geological Survey
P.O. Box 25046, DFC, MS 966
Denver, Colorado 80225-0046
(K.E.A., R.W.J., J.W.G., F.K.R.)

University of Canterbury
Private Bag 4800
Christchurch 8140
New Zealand
(B.B., J.D., M.V.)

University of Washington
132F More Hall
Seattle, Washington 98195
(J.W.)

University of Sheffield
Western Bank
Sheffield S10 2TN
United Kingdom
(D.N.P.)

Massey University
Private Bag 11 222
Palmerston North 4442
New Zealand
(S.M.)

Manuscript received 11 October 2017;
Published Online 27 March 2018

Table A1

Summary of Data Used to Compile the Landslide Inventory

	Item	Data	Type	Date (NZST)	Source	Ground Resolution (m)	Public Availability	Notes
Pre-Kaikoura earthquake data	1	Kaikoura District aerial photographs	Orthorectified mosaics	2014–2015	Environment Canterbury (ECAN) (captured by Aerial Surveys)	0.3	Yes	
			Individual tiled tiffs (provided by Council) converted to one mosaic by GNS Science					
	2	Marlborough District aerial photographs	Orthorectified mosaic	2011–2012	Marlborough District Council (MDC) (captured by Aerial Surveys)	0.4	Yes	
			Individual tiled tiffs (provided by Council) converted to one mosaic by GNS Science					
		Marlborough District aerial photographs	Orthorectified mosaic	2015–2016	MDC, captured by AAM Group Ltd	0.2	Early 2018	
			Individual tiled tiff format files					
	3	Kaikoura digital surface model (DSM), generated from the photographs taken for 1 and 2	ESRI grid file	2014–2015	ECAN, captured by Aerial Surveys Ltd	1.0	Early 2018	
	4		ESRI grid file already provided	2014–2015	ECAN, captured by Aerial Surveys Ltd	10.0	Early 2018	
	5	Airborne lidar	Point clouds converted to DEMs and hillshades by GNS Science	2012	Captured by AAM Group Ltd	1.0	Yes	Only the coastal strip from Ward through to Cheviot
Post-Kaikoura earthquake data	5	WorldView-2 satellite imagery	Multispectral bands supplied raw. Orthorectified as an Imagine file and converted to mosaics by GNS Science	22 November 2016	Captured by Digital Globe	2.4	Yes	Eagle technology processed the same raw images and provided to all of government
	6	WorldView-3 satellite imagery		15 November 2016	Captured by Digital Globe	1.4	Yes	
	7	GeoEye satellite imagery		15 November 2016	Captured by Digital Globe	2.0	Yes	
	8	Aerial photographs	RGB stereo-tiff files with image coordinates, processed to individual orthorectified images and DSMs by GNS Science	December 2016	Captured by Aerial surveys Ltd. commissioned by LINZ at the request of GNS Science and other New Zealand agencies	0.3	Early 2018	Area covered is the main area affected by landslides and the total area affected by landslides

(*continued*)

Table A1 (*Continued*)

Item	Data	Type	Date (NZST)	Source	Ground Resolution (m)	Public Availability	Notes
9	Airborne lidar	Aerial Surveys to provide complete processed data set Point clouds converted to DEM and hillshades by GNS Science	November–December 2016	Captured by AAM Group Ltd. commissioned by LINZ at the request of GNS Science and other New Zealand agencies	1.0	On request	Only the coastal strip, main faults, and Goose Bay provided to date. Additional areas (dam sites) to be provided later
10	Terrestrial lidar of landslides and landslide dams on the rivers called Hapuku, Ote Makura, Linton, Conway, Towy, Stanton, and Leader	Point clouds, orthorectified images	November and December 2016 March, April, May, and September 2017	Captured by GNS Science	Variable	Yes	Multiple surveys of each dam. Several of the dams failed following cyclones Debbie and Cook, and surveys of these dams were carried out post failure

NZST, New Zealand Standard Time; lidar, light detection and ranging; LINZ, Land Information New Zealand.

Table A2

VIF Matrix for the Variables Included in the Logistic Regression Models

Variables	LSR	$Slope_{MEAN}$	$Elev_{MEAN}$	FaultDist	PGV_{MEAN}	$PGV_{BRADLEY}$	PGV_{LF}	PGV_{SM}	PGA_{SM}
LSR	—	4.54	1.60	1.00	1.01	1.03	1.03	1.13	1.00
$Slope_{MEAN}$		—	1.48	1.00	1.00	1.03	1.03	1.16	1.00
$Elev_{MEAN}$			—	1.04	1.00	1.00	1.02	1.11	1.02
FaultDist				—	1.10	1.04	1.02	1.30	1.60
PGV_{MEAN}					—	8.89	3.04	1.09	1.16
$PGV_{BRADLEY}$						—	1.96	1.00	1.05
PGV_{LF}							—	1.00	1.03
PGV_{SM}								—	1.62
PGA_{SM}									—

VIF values greater than 10 indicate a high level of multicollinearity (Kutner *et al.*, 2004) and are avoided in our models. LSR, local slope relief.